Ice particle impact on solid walls: size modeling of reemited fragments

Jean-Mathieu Senoner, Pierre Trontin, Louis Reitter, Norbert Karpen, Markus Schremb, Mario Vargas, Philippe Villedieu

Ice particle impact on solid walls: size modeling of reemited fragments

Jean-Mathieu Senoner[a,*], Pierre Trontin[a], Louis Reitter[b], Norbert Karpen[b,c], Markus Schremb[b], Mario Vargas[d], Philippe Villedieu[a]

[a] *ONERA/ DMPE, Université de Toulouse, F-31055 Toulouse, France*
[b] *Technische Universität Darmstadt/ Institute for Fluid Mechanics and Aerodynamics, Alarich-Weiss-Strasse 10, D-64287 Darmstadt, Germany*
[c] *Airbus Central Research and Technology/ Aerodynamic Efficient Surfaces, Willy-Messerschmitt-Strasse 1, D-82024 Taufkirchen, Germany*
[d] *NASA Glenn Research Center/ Icing Branch, 21000 Brookpark Rd, Cleveland, Ohio 44135, United States*

Abstract

The present work deals with ice particle fragmentation resulting from impact on a solid wall. First, a semi-empirical model to predict the size of the largest reemited fragment is presented. It is based on the energy-horizon theory of fragmentation developed by Grady (*J. Mech. Phys. Sol., 36(3),353-384, 1988*) in combination with a strain rate scaling based on the indentation radius formed upon impact. Model predictions are in good agreement with experimental data from six different sources.

In addition, an empirical fit to the ice fragment volume distribution is sought. Different candidate fits, namely power law, Weibull and lognormal are proposed and evaluated both qualitatively and quantitatively. The fragment volume distributions appear to exhibit different trends for impact conditions representative of ice crystals and hailstones. For this reason, a less

*Corresponding author, jean-mathieu.senoner@onera.fr

accurate yet more robust power law fit is proposed to model the available fragment volume distribution data.
Keywords: ice crystal icing, impact, fragmentation, energy-horizon theory, maximum fragment diameter, fragment volume distribution

1. Introduction

Ice crystal icing of civil aircrafts generally occurs in the vicinity of deep convective clouds at cruise altitudes [1]. Ice crystals, whose diameters range between 5 µm and 2 mm approximately, may adhere to the surfaces they impinge on when the latter are heated or when the crystals themselves are partially melted [2]. Thus, ice crystal icing necessarily occurs within the engine, where significant fragmentation occurs as impact velocities are comprised between $50\,\mathrm{m\,s^{-1}}$ to $250\,\mathrm{m\,s^{-1}}$ approximately. The associated size reduction enhances melting, enabling the sticking of ice fragments on engine walls and favoring ice accretion. The latter may cause aerodynamic blockage, mechanical damage due to ice block detachment or even flameout. For this reason, ice crystal icing still represents a serious threat to aviation safety [3, 4, 5] and the characterization of reemited fragment properties is a necessary ingredient to improve the predictive capabilities of numerical icing tools [6, 7].

Several experiments reproducing impact conditions representative of ice crystal icing were recently conducted. Hauk *et al.* [8] characterized the impacts of both spherical and nonspherical ice particles within a large size (30 µm - 3.5 mm) and a moderate normal impact velocity range (5 - $70\,\mathrm{m\,s^{-1}}$). Considering the portions of the crystal volumes shattered into fragments as well as the distinct disintegration patterns in their experiments, Hauk *et*

al. [8] proposed to classify fragmentation into minor, major and catastrophic regimes.

Vargas *et al.* [9] carried out spherical ice particle impacts on a flat glass plate. The authors characterized ice particle diameters and velocities before impact. In addition, they placed a high resolution camera under the glass plate to capture the fragment contours and reported that the resulting fragment number distributions could be well approximated by lognormal laws.

Experiments dedicated to the characterization of hailstone fragmentation [10, 11] consider normal impact velocities up to $200\,\mathrm{m\,s^{-1}}$ and ice particle diameters ranging from 5 to 27.5 mm. In order to determine the validity limits of the models proposed in the current work, measurements from hailstone impact experiments are added to the validation database. Pan and Render [10] examined the fragmentation of hailstone sized ice particles on a flat plate. Among others, they derived empirical correlations to determine the fragments' maximum diameter and proposed to model the reemited fragment volume distribution with a Weibull law. Guégan *et al.* [11] performed impact experiments of hailstone sized ice particles on a glass plate. They found the ratio of the average radial fragment velocity to the normal impact velocity to be approximately constant. From the same experiments, Guégan *et al.* [11] also provided unpublished size distribution data to the authors [12], which will be used for validation purposes.

Tippman *et al.* [13] performed detailed numerical simulations of the impact of a hailstone sized ice particle on a rigid surface to reproduce their own experimental measurements for the force history resulting from such impact. They propose to distinguish between two main impact phases:

elastic-dominated structural response followed by cracking/ fragmentation. Performing numerical simulations of the impact of brittle spheres using the Discrete Element Method (DEM), Carmona *et al.* [14] reported that cracks formed within the particle in the region above a compressive cone delimited by the indentation radius formed upon impact. They also found the largest radial and circumferential stresses to occur in a ring shaped area delimiting the outer contact zone between particle and substrate, leading to the propagation of meridional cracks. Hauk *et al.* [8] also conclude that meridional cracks drive major and catastrophic fragmentation, while they assume lateral crack formation to dominate at lower impact velocities.

Despite the numerous insights gained from these research efforts, current models predicting the properties of the reemited fragments remain essentially empirical. Villedieu et al. [15] proposed an empirical model yielding size and velocity properties of the reemited fragments based on regression fits to various experimental data. Guégan *et al.* [11] provide correlations for the radial and normal velocities of the reemited fragments while Pan and Render [10] propose a Weibull fit for the reemited fragment volume distribution. On the contrary, Weiss [16] reports that ice fragment size distributions follow power-laws.

The present work aims at deriving a model for the size of the largest reemited fragment based on a simple energy principle. First, a semi-empirical model relying on the energy-horizon theory of fragmentation [17, 18] is used to predict the maximum fragment size. The current model is closed via a strain rate scaling from the literature [19, 20] based on the indentation radius formed upon impact. The consistency of the model predictions is

demonstrated by comparison with a large experimental database. Then, the available fragment volume distribution data is examined. Different fits to the fragment volume distribution are proposed, namely power, lognormal and Weibull law. These fits are compared both qualitatively and quantitatively. The main findings and outlooks are summarized in the conclusion.

2. Maximum fragment size modeling

2.1. Energy based fragmentation model

The main assumptions governing the choice of the current model, which will be further justified below, were those of a dynamic and brittle fragmentation process. Furthermore, a simple and tractable model suitable for application purposes, hence based on a limited set of global impact parameters, was sought. In particular, the current model for the maximum reemited fragment size relies on an energy conservation principle between the initial and end states of fragmentation [17, 18]. It states that the energy contributions fuelling fragmentation, namely elastic and kinetic energies, must exceed the energy required to create new fracture surface at the local scale. The modeling framework is completed using two additional hypotheses:

- first, a correlation distance set by the product of the crack propagation speed, taken as the speed of sound, and the characteristic time scale of fragmentation is defined. This correlation distance sets the upper bound on the fragment size.

- second, a uniform dilatational expansion within the body under consideration is assumed

The resulting equation system then writes:

$$s \leq 2ct \tag{1}$$

$$\frac{1}{2}\frac{P_s^2}{\rho c^2} + \frac{1}{120}\rho\dot{\varepsilon}^2 s^2 \geq \frac{6G_c}{s} \tag{2}$$

$$P_s = \rho c^2 \dot{\varepsilon} t \tag{3}$$

In eq. 1, s denotes the characteristic correlation distance/ fragment size, t the time variable, while the crack propagation velocity is given by the speed of sound c. The latter is evaluated as:

$$c = \sqrt{\frac{E}{\rho}} \tag{4}$$

with $E = 10.5 \times 10^9\,\mathrm{Pa}$ the Young modulus and $\rho = 917\,\mathrm{kg\,m^{-3}}$ the material density of ice[1], which may both be assumed constant [21]. The resulting crack propagation speed appears to exceed the value reported by Tippman *et al.* [13], i.e. approximately $2000\,\mathrm{m\,s^{-1}}$, by almost 70% and should thus rather be considered as providing the correct order of magnitude. Equation 2 represents the energy balance between the contributions fuelling fragmentation, namely the elastic and kinetic energies on the left-hand side, which must exceed the energy required to create new fracture surface on the right-hand side. In eq. 2, P_s denotes the tensile pressure, $\dot{\varepsilon}$ the strain rate and G_c the energy per unit area required to create new fracture surface. While the latter is assumed constant in the standard formulation of the model, with $G_c = G_{c,0} = 0.12\,\mathrm{J\,m^{-2}}$ [22], a relation allowing to account for its temperature dependency is provided in Appendix A. Finally, eq. 3 describes the time history of tensile pressure leading to failure.

[1] all physical parameters/ constants are written in SI units

Writing eqs. 1 and 2 as equalities, the characteristic fragment size follows a power law on the strain rate when combining eqs. 1-3:

$$s = K\dot{\varepsilon}^{\alpha} \tag{5}$$

with $K = (45G_c/\rho)^{1/3}$ and $\alpha = -2/3$, a result characteristic of highly dynamic fragmentation [23]. In addition, the lower bound $\alpha = -1$ may be derived for quasi-static loadings [18].

Following Glenn and Chudnovsky [23], two normalization parameters are defined for the fragment size and the strain rate:

$$s_0 = 12\, EG_c\, P_{s,0}^{-2} \tag{6}$$

$$\dot{\varepsilon}_0 = \frac{1}{6}\, P_{s,0}^{3}\, c^{-3}\, \rho^{-2}\, G_c^{-1} \tag{7}$$

with the constant reference tensile pressure set to $P_{s,0} = 1 \times 10^6\,\mathrm{Pa}$. Using these expressions, eq. 5 may be rewritten in the following dimensionless form:

$$\frac{s}{s_0} = C_f \left(\frac{\dot{\varepsilon}}{\dot{\varepsilon}_0}\right)^{\alpha} \tag{8}$$

where C_f is a dimensionless parameter to be adjusted to available experimental data. The characteristic strain rate required for closure is presented in the following.

2.2. Strain rate estimate

A sketch of the envisioned fragmentation mechanism is shown in fig. 1. It is assumed that the early instants of impact are characterized by a rigid body motion of the particle while the latter is plastically deformed/ crushed in the contact area with the solid surface (top view of fig. 1). The assumption

of plastic deformation within the contact area is in line with the constitutive laws used to model the mechanical behavior of ice [24] and numerical simulations of ice particle impact [13, 25]. Furthermore, it is assumed that the strong compressive deformation of the crystal remains restricted to the immediate vicinity of the contact area with the solid wall, whereas the remaining part of the crystal is subject to significant strain, eventually leading to its fragmentation via crack propagation (bottom view of fig. 1). This assumption is consistent with the respective impact and crack propagation speeds, the latter corresponding to the speed of sound and thus being an order of magnitude larger than the former. It also seems in line with the numerical simulations of brittle sphere impacts reported by Carmona *et al.* [14] as they observe crack initiation due to increasing tensile radial and circumferential stresses in a ring shaped region above the strongly compressive contact area. Contrary to compression, the tensile failure of ice shows brittle behavior and a negligible influence of strain rate [21], in agreement with the interpretation of the fragmentation process outlined in section 2.1.

Following Hutchings [19], the characteristic strain driving fragmentation is assumed to scale as the ratio of the indentation radius a to the initial particle diameter D_0:

$$\varepsilon \sim \frac{a}{D_0} \tag{9}$$

Assuming plastic deformation in the contact area, Roisman and Tropea [20] found the indentation radius a to scale as:

$$a \sim U_{n,0}^{1/2} \, D_0 \, \rho^{1/4} \, Y_c^{-1/4} \tag{10}$$

with $U_{n,0}$ being the normal impact velocity and Y_c the compressive yield strength of ice. Hutchings [19] obtained the same result as in eq. 10 but used

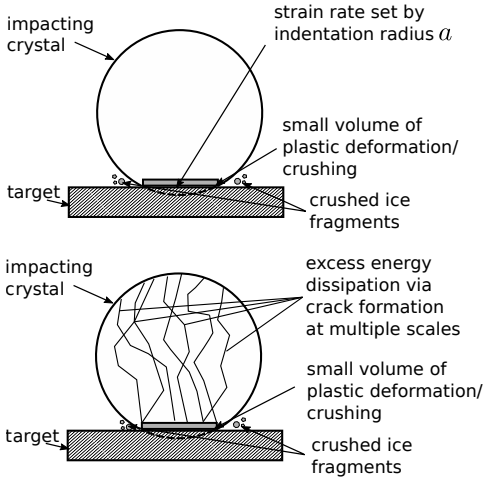

Figure 1: Sketch of the envisioned two main fragmentation steps. Above: early instants of impact, where the area of contact between the crystal and the surface is plastically deformed /crushed. Below: the tensile strain level within the crystal is determined by the indentation radius, leading to crack formation, propagation and eventually fragmentation.

a quasi-static indentation hardness to characterize the material's compressive resistance. The strain scaling in eq. 9 is then divided by the time necessary to form the indentation [20]:

$$t_i \sim D_0 \, \rho^{1/2} \, Y_c^{-1/2} \tag{11}$$

Combining eqs. 9-11 finally yields:

$$\dot{\varepsilon} \sim U_{n,0}^{1/2} \, D_0^{-1} \, \rho^{-1/4} \, Y_c^{1/4} \tag{12}$$

In the standard formulation, a constant quasi-static value is used for the compressive yield strength, $Y_c = Y_{c,0} = 5.2 \times 10^6\,\mathrm{Pa}$. Relations allowing to account for the strain rate and temperature dependency of this parameter are provided in Appendix A.

2.3. Validation

The model predicting the size of the largest fragment given by eq. 8 in conjunction with eq. 12 is evaluated using a large experimental dataset compiling data of Karpen *et al.* [26], Reitter *et al.* [27], Hauk *et al.* [8], Vargas *et al.* [9], Pan and Render [10] and previously unpublished data of Guégan *et al.* [12]. For the experiments of Hauk *et al.* [8] and Karpen *et al.* [28], data characterizing impacts without fragmentation were discarded. Also, size measurement data is only available for a subset of the fragment velocity data published by Guégan *et al.* [11]. Finally, the raw experimental data was not accessible for the experiments of Pan and Render [10] and was hence retrieved by digitizing the curves from their article.

The resulting ranges for the normal impact velocities, initial diameters and initial particle temperatures of each experiment are summarized in table 1. In addition, the ranges spanned by two nondimensional numbers commonly used to characterize ice particle fragmentation thresholds in the literature are also provided. The nondimensional parameter ξ was introduced by Hauk *et al.* [8] to estimate the probability of fragmentation:

$$\xi = \frac{U_{n,0} D_0^{2/3}}{\beta} \tag{13}$$

with $\beta = 0.14\,\mathrm{m}^{5/3}\,\mathrm{s}^{-1}$. The probability of fragmentation approaches zero for $\xi \to 0$ while the probability of catastrophic fragmentation tends to one for $\xi > 1.1$ [8]. Vidaurre and Hallet [22] define a nondimensional impact parameter relating the kinetic energy upon impact to the surface energy:

$$\mathcal{L} = \frac{1}{12} \frac{\rho U_{n,0}^2 D_0}{G_c} \tag{14}$$

Variable Units	$U_{n,0}$ ($\mathrm{m\,s^{-1}}$)	D_0 (mm)	T_0 (K)	ξ (-)	$\mathcal{L} \times 10^3$ (-)
Karpen *et al.* [26]	[5-75]	[0.02-0.45]	255	[0.3-2.2]	[0.06-0.8]
Reitter *et al.* [27]	[7-74]	[1.3-4.5]	[258-263]	[0.9-9.3]	[0.07-6.0]
Hauk *et al.* [8]	[15-70]	[0.08-3]	248	[0.5-3.5]	[0.08-2.9]
Vargas *et al.* [9]	[22-65]	[2.3-2.6]	266	[2.8-8.7]	[2.3-21.4]
Pan and Render [10]	[60-150]	[12.7-19]	233	[23.3-76.3]	[48.9-457]
Guégan *et al.* [12]	[40-203]	6.2	255	[9.7-31.6]	[7.7-124.1]

Table 1: Main impact parameter ranges of the experimental data used for validation. For different reasons exposed in the present section, the data used for validation consists of a subset of the original data for the experiments of Karpen *et al.* [26], Hauk *et al.* [8] and Guégan *et al.* [12] (previously unpublished data for the latter).

The threshold for major/ catastrophic fragmentation is generally set to $\mathcal{L}_2 = 90$ [15]. Considering the orders of magnitude of ξ and $\mathcal{L}$ in table 1, all impact experiments performed by Vargas *et al.* [9], Pan and Render [10] and Guégan *et al.* [12] lie well within the catastrophic fragmentation regime. On the contrary, impact outcome classifications performed by Karpen *et al.* [28] and Hauk *et al.* [8] confirm that their experiments also comprise minor and major fragmentation impacts. Thus, the present experimental data covers all fragmentation regimes according to the classification of Hauk *et al.* [8].

First, the correlation of the maximum fragment diameter with the proposed strain rate estimate is examined. For this purpose, the scaling in eq. 12 is interpreted as an equality with a unitary constant. In order to validate the assumption that the maximum fragment diameter and strain rate are linked by a power law relation, the data is plotted on a log-log scale. Because they

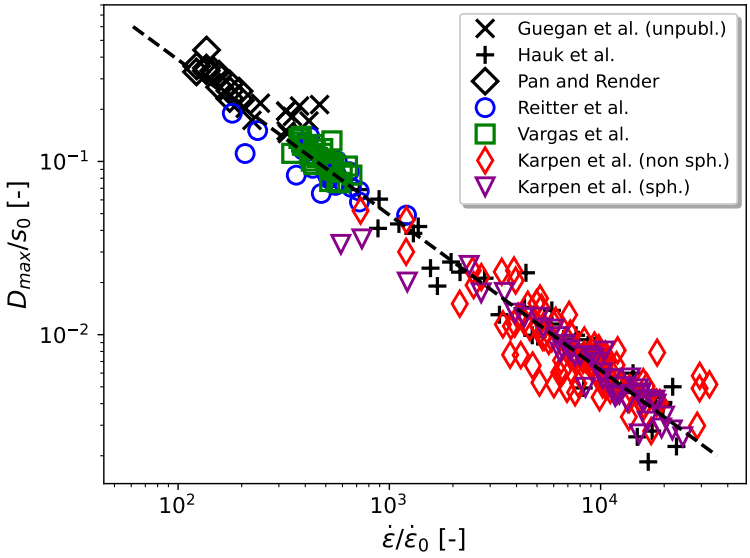

Figure 2: Experimental normalized maximum fragment diameter over the normalized strain rate for the experimental data of Karpen *et al.* [26], Reitter *et al.* [27], Hauk *et al.* [8], Guégan *et al.* [12] (previously unpublished data) and Pan and Render [10] on a log-log scale. For the experimental dataset of Karpen *et al.* [26], the impact data was split into initially spherical ("sph.") and non-spherical ("non sph."). The regression curve to the entire dataset ($\ln(D_{max}/s_0) \approx -0.896 \ln(\dot{\varepsilon}/\dot{\varepsilon}_0) + 3.175$) is displayed as a black dashed line.

contain significantly more datapoints, only one out of respectively six and ten datapoints is plotted for the experiments of Reitter *et al.* [27] and Karpen *et al.* [26]. The result is displayed in fig. 2 and illustrates an excellent correlation as all experimental datapoints approximately collapse on the linear regression curve. From a regression to the entire experimental dataset, the exponent α and the multiplicative constant C_f of the semi-empirical model are obtained as:

$$\alpha \approx -0.896 \tag{15}$$

$$C_f \approx 23.936 \tag{16}$$

Note that these model parameters are obtained assuming both the fracture surface energy per unit volume and the compressive yield strength to be constant, respectively $G_c = G_{c,0} = 0.12\,\mathrm{J\,m^{-2}}$ and $Y_c = Y_{c,0} = 5.2 \times 10^6\,\mathrm{Pa}$. Modeling the variations of G_c with temperature and of Y_c with both temperature and strain rate, see Appendix A, yields:

$$\alpha_v \approx -0.885 \tag{17}$$

$$C_{f,v} \approx 42.824 \tag{18}$$

Thus, variations of G_c and Y_c mostly affect the value of the multiplicative constant of the model, but not its exponent. Further analysis shows that the temperature dependencies of these material properties have a negligible influence on the increase of $C_{f,v}$ with respect to C_f. Thus, this significant raise is mostly due to the nonlinear dependency of the compressive yield strength Y_c on the strain rate, see eqs. A.2 and A.3, as well as the choice of a quasi-static reference value for the latter in the model formulation based on constant

material properties. While the value for the exponent α lies within the expected bounds, i.e. -1 (quasi-static loading) and $-2/3$ (dynamic loading), see section 2.1, it was expected to lie somewhat closer to the upper bound characteristic of highly dynamic loadings. Despite this fact, the quantitative agreement with the different experimental data appears very satisfactory, as may be seen in table 2, which provides the average modeling errors for each dataset. As for the plot in fig. 2, the experimental data of Karpen *et al.* [26] was split into initially spherical and non spherical particles to assess the influence of the initial shape on modeling accuracy. In order to further assess the accuracy of the present model, average errors are also computed for the models of Villedieu *et al.* [15] and Pan and Render [10]. The model of Villedieu *et al.* [15] expresses the maximum fragment diameter as a power of the Vidaurre number (eq. 14) to its threshold value for fragmentation with a constant exponent:

$$D^{v}_{max}/D_0 = \left(\frac{\mathcal{L}_2}{\mathcal{L}}\right)^{2/11} \tag{19}$$

The model of Pan and Render [10] reads:

$$D^{pr}_{max}/D_0 = 0.437 - 0.922\left(\frac{U_{n,0}}{a_L}\right) \tag{20}$$

with a nondimensionalization constant taken as the speed of sound in air at ambient temperature, i.e. $a_L = 340\,\mathrm{m\,s^{-1}}$. Since eq. 20 is only meaningful for $U_{n,0} < 161\,\mathrm{m\,s^{-1}}$, it becomes invalid for the largest impact velocity experiments of Guégan *et al.* [12]. Finally, the average errors obtained with varying fracture surface energy and compressive yield strength are given in parenthesis. The values of the latter indicate that uncertainties on material properties do not significantly affect the precision of the present model.

The accuracy of the present model appears good for all datasets, the lowest average error amounting to 12.6 % (both Pan and Render [10] and Vargas *et al.* [9]) and the largest to 26.3 % for the nonspherical impact data of Karpen *et al.* [26]. Error levels between the present model and the model of Villedieu *et al.* are comparable for the datasets of Hauk *et al.* [8] and Guégan *et al.* [12]. On the contrary, the present model performs better than the model of Villedieu *et al.* [15] for the datasets of Karpen *et al.* [26], Vargas *et al.* [9] and Pan and Render [10], with error reductions ranging between 5 and 11 %. As expected, the model of Pan and Render [10] performs best for their own experimental data and its error levels with respect to the other models remain similar for the data of Reitter *et al.* [27] and Guégan *et al.* [12]. For the remaining data, the model of Pan and Render [10] displays much larger average error levels. For the current model, the average errors do not seem to correlate with the main impact parameters as it performs similarly well for ice crystal and hailstone sized particles. On the contrary, it displays a significant increase in error levels when considering impacts of nonspherical particles. Such behavior could be expected as impacts of irregular particles are more difficult to model due to contact area variations and associated rotation effects. A more visual illustration of the present model accuracy is provided in fig. 3, where the modeled maximum fragment diameters are directly compared to experimental data in a scatterplot. While the model appears accurate on average, significant errors may be noted for single impact events.

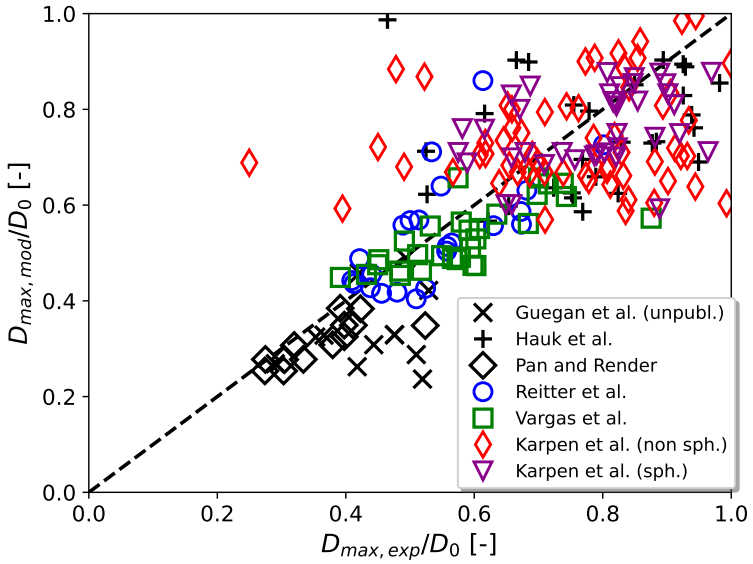

Figure 3: Experimental maximum fragment diameter normalized by the initial diameter plotted over the current model values for the different experimental data. For the experimental dataset of Karpen *et al.* [26], the impact data was split into initially spherical ("sph.") and non-spherical ("non sph.") particles.

Experiment	Particle shape	Current model avg. error [%]	Villedieu *et al.* [15] avg. error [%]	Pan and Render [10] avg. error [%]
Karpen *et al.* [26]	sph.	17.1 (17.2)	28.2	44.7
Karpen *et al.* [26]	non sph.	26.3 (26.4)	31.6	46.4
Reitter *et al.* [27]	sph.	16.1 (16.1)	14.7	19.2
Hauk *et al.* [8]	mixed	23.0 (23.0)	26.5	45.7
Vargas *et al.* [9]	sph.	12.6 (12.8)	20.9	27.0
Pan and Render [10]	sph.	12.6 (7.9)	21.3	7.8
Guégan *et al.* [12]	sph.	23.6 (23.1)	24.1	24.2

Table 2: Average errors of the maximum fragment diameter obtained with the current model (the numbers in parentheses correspond to the average errors obtained with varying material parameters, see Appendix A), the model of Villedieu *et al.* [15] and the model of Pan and Render [10], each compared with data from the different experimental datasets.

3. Fragment size distribution

Fracture in brittle solids is weakly dissipative and may thus proceed on successively finer scales to dissipate the excess energy [29]. If the fragmentation process is further considered scale invariant, it may be described using fractal theory. Size distributions resulting from fractal fragmentation processes follow power laws [30], also known as Dinger-Funk distributions [31], and the latter were reported to accurately reproduce fragment size distributions in many experiments [16, 32].

Considering ice fragmentation more specifically, size distributions indicating fractal behavior were reported for uniaxial compression creep, crushing and indentation experiments [16]. On the other hand, the numerical simulations of brittle sphere impacts of Carmona *et al.* [14] indicate that only the smaller fragments follows a power law distribution. Thus, the authors chose a Weibull law to model their numerical fragment mass distributions, as do Pan and Render [10] for their hailstone impact experiments. Finally, Vargas *et al.* [9] report that the fragment number distributions are well approximated by lognormal laws in their ice particle impact experiments, indicating that the fragmentation process could be interpreted as the production of large fragments successively and randomly split into smaller fragments [33]. From the above discussion, it appears that the best candidate fit to the present size distribution data is unknown *a priori*.

Following a brief description of the available experimental size distribution data, the method used to derive power, Weibull and lognormal fits to the latter is presented. The predictions of these fits are then compared qualitatively and quantitatively.

3.1. Experimental data

Within the present dataset, three experiments provide information on the fragment size distribution resulting from impact, namely Reitter *et al.* [27], Vargas *et al.* [9] and previously unpublished size fragment data [12] from the experiments of Guégan *et al.* [11]. Vargas *et al.* [9] and Guégan *et al.* [12] obtain their size distribution measurements via high resolution images of the fragments once they have come to rest on the impinged surface. Reitter *et al.* [27, 34] detect the contour of the reemited fragments in motion and track each fragment separately. The raw experimental data is not available for the experiments of Guégan *et al.* [12], but only the number and volume size distributions discretized over 80 bins. For the experiments of Reitter *et al.* [27] and Vargas *et al.* [9], the raw data consists of approximately 200 and 2000 fragment size measurements per impact experiment. The impact parameter ranges are identical to those reported in table 1 in section 2.3. Hence, the data of Vargas *et al.* [9] and Guégan *et al.* [12] entirely lie in the catastrophic fragmentation regime. While the experimental data of Reitter *et al.* [27] also cover minor and major fragmentation, only a few data of their data points lie in the latter regimes, which is insufficient to warrant meaningful conclusions. Thus, the analysis presented in the following only applies to the catastrophic fragmentation regime.

3.2. Candidate fitting distributions

When considering ice accretion, impact dynamics are driven by particle inertia as larger particles are more likely to impinge on solid walls within the engine. Further assuming broad size distributions, smaller particles may be expected to carry a negligible amount of mass and thus not to significantly

contribute to the accretion process. For this reason, a fit to the fragment volume distribution is sought.

The definitions of the fragment diameter moments in the literature are generally based on the number distribution p_n:

$$D_{ij}^n = \left(\frac{\int_0^\infty p_n(D) D^i dD}{\int_0^\infty p_n(D) D^j dD} \right)^{\frac{1}{i-j}} \tag{21}$$

with i and j integer numbers. As the focus lies on statistical quantities characteristic of the largest fragments, a fit accurately matching the Sauter mean diameter D_{32}^n and the mean volume diameter D_{43}^n is sought. In addition, the volume median diameter D_{50}^v separating 50% of the fragment volume from the 50% remaining, is used. Similarly, the D_{10}^v and D_{90}^v diameters are also employed.

Power, Weibull and lognormal laws are examined as candidate fits to the present fragment volume distribution data in the following. They are respectively defined as:

$$p_{p,v}(D) = \frac{\gamma + 1}{D_{max}^{\gamma+1} - D_{min}^{\gamma+1}} D^\gamma \tag{22}$$

$$p_{ln,v}(D) = \frac{1}{\sqrt{2\pi} D \sigma_{ln}} \exp\left(-\frac{(\ln(D) - \mu_{ln})^2}{2\sigma_{ln}^2} \right) \tag{23}$$

$$p_{wb,v}(D) = \frac{\beta}{\lambda} \left(\frac{D}{\lambda} \right)^{\beta-1} \exp\left(-\left(\frac{D}{\lambda} \right)^\beta \right) \tag{24}$$

with γ, D_{min}, D_{max} respectively representing the exponent, lower and upper bound of the power law in eq. 22, where the upper bound D_{max} is deduced from the model presented in section 2. In eq. 23, μ_{ln} and σ_{ln} denote the logarithmic mean and variance of the lognormal law while λ and β respectively represent the scale and shape parameters of the Weibull law in eq. 24.

The power law, Weibull and lognormal laws have analytical expressions for their (volume based) moments:

$$D^v_{ij,p} = \left[\frac{\gamma+j+1}{\gamma+i+1}\frac{(D^{\gamma+i+1}_{max}-D^{\gamma+i+1}_{min})}{(D^{\gamma+j+1}_{max}-D^{\gamma+j+1}_{min})}\right]^{\frac{1}{i-j}} \quad (25)$$

$$D^v_{ij,ln} = \exp(\mu_{ln})\left[\exp\left(\frac{\sigma^2_{ln}}{2}(i+j)\right)\right]^{\frac{1}{i-j}} \quad (26)$$

$$D^v_{ij,wb} = \lambda\left[\left(\frac{\Gamma(1+\frac{i}{k})}{\Gamma(1+\frac{j}{k})}\right)\right]^{\frac{1}{i-j}} \quad (27)$$

Noting that volume and number distributions are linked as $p_v(D)dD \sim p_n(D)D^3dD$, their repective diameter moments may be related as:

$$D^v_{i-3\,j-3} = D^n_{ij} \quad (28)$$

3.3. Parameter evaluation of the candidate fitting distributions

The most accurate fits to the present fragment volume distribution data were obtained when using the current strain rate estimate to model the Sauter mean and mean volume diameters of the fragments first and then computing the associated distribution parameters. This is because no clear correlation of the parameters driving the shapes of the distributions, namely γ, σ_{ln} and β, could be found with respect to the impact parameters. On the contrary, the Sauter mean and mean volume diameters of the fragments appear to correlate rather well with the current strain estimate (based on constant material properties), as may be seen from figs. 4 and 5.

While the regression curves indicate a somewhat poorer correlation compared to the maximum diameter, reasonably accurate fits to these quantities may be proposed for the data of Reitter *et al.* [27] and Vargas *et al.* [9]. On

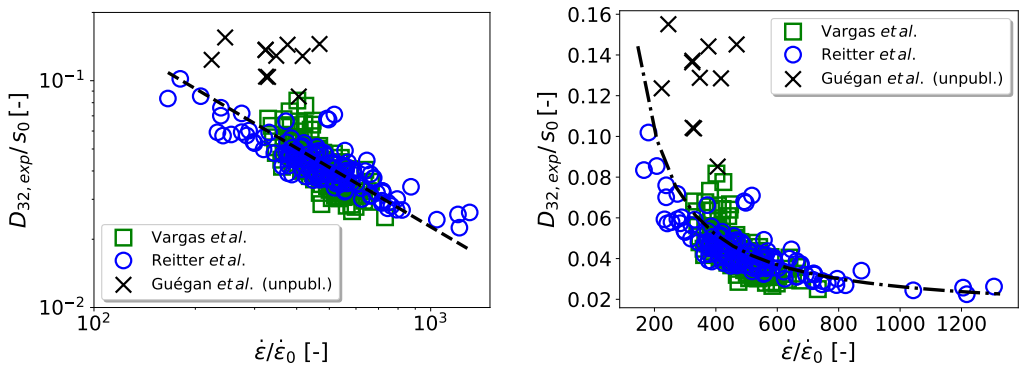

Figure 4: Left: regression curve $(\ln(D_{32}^n/s_0) \approx -0.872 \ln(\dot{\varepsilon}/\dot{\varepsilon}_0) + 2.237)$ displayed as a dashed black line on a log-log scale of the Sauter mean diameter over the strain rate estimate given by eq. 12. Right: Evolution of the Sauter mean diameter over the strain rate estimate and proposed fit (dash-dotted black line).

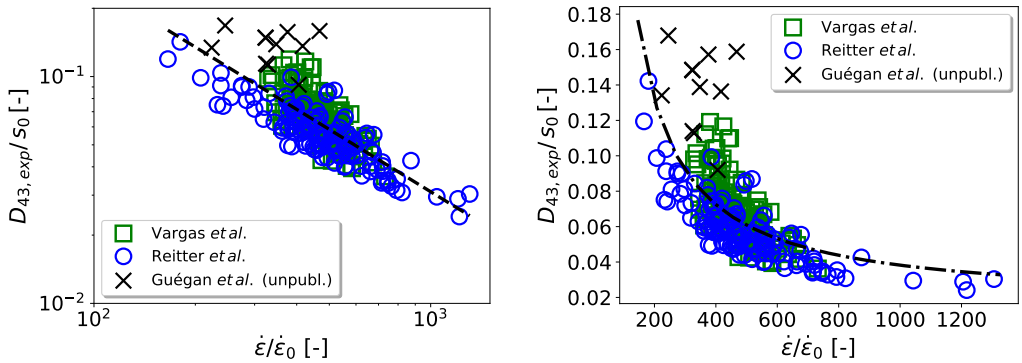

Figure 5: Left: regression curve $(\ln(D_{43}^n/s_0) \approx -0.912 \ln(\dot{\varepsilon}/\dot{\varepsilon}_0) + 2.831)$ displayed as a dashed black line on a log-log scale of the volume mean diameter over the strain rate estimate given by eq. 12. Right: Evolution of the volume mean diameter over the strain rate estimate and proposed fit (dash-dotted black line).

Experiments	D_{32}^n average fitting error [%]	D_{43}^n average fitting error [%]
Reitter *et al.* [27]	13.87	20.42
Vargas *et al.* [9]	14.89	14.54
Guégan *et al.* [12]	35.09	48.17

Table 3: Average errors on the Sauter mean diameter D_{32} and volume weighted mean diameter D_{43} for the different experiments using the fits given in eqs. 29 and 30

the contrary, poor agreement is obsverved for the data of Guégan *et al.* [12] which displays significantly larger values for both the Sauter mean diameter and mean volume diameter in comparison to the data of Reitter *et al.* [27] and Vargas *et al.* [9] for comparable strain rates. It is interesting to note that the regression slopes obtained for these quantities, respectively -0.872 for the Sauter mean diameter and -0.912 for the mean volume diameter, are close to the value obtained for the maximum diameter, i.e. $\alpha \approx -0.896$ for constant material properties. In addition, an asymptotic behavior seems visible for these quantities at the largest strain rates, such that a constant is added to the current fits. In order to further minimize the average error of the fits, it is chosen not to constrain their exponents, yielding:

$$\frac{D_{32}^n}{s_0} = C_{f,32} \left(\frac{\dot{\varepsilon}}{\dot{\varepsilon}_0} \right)^{\alpha_{32}} + a_{0,32} \tag{29}$$

$$\frac{D_{43}^n}{s_0} = C_{f,43} \left(\frac{\dot{\varepsilon}}{\dot{\varepsilon}_0} \right)^{\alpha_{43}} + a_{0,43} \tag{30}$$

with respectively, $C_{f,32} \approx 58.682$, $\alpha_{32} \approx -1.266$, $a_{0,32} \approx 0.020$ and $C_{f,43} = 29.997$, $\alpha_{43} = -1.051$, $a_{0,43} \approx 0.171$. The average error levels with respect to the experimental values of these parameters are provided in table 3.

The parameters of the lognormal and Weibull distributions are separable

in eqs. 26 and 27 and may thus be directly determined from relations 29 and 30. On the contrary, the parameters of the power law fit D_{min} and γ are not separable in eq. 25 and the dedicated method used to determine the latter is presented below. Note that all distributions are renormalized when necessary to prevent the prediction of fragment volume beyond the maximum diameter estimate presented in section 2.

3.4. Determination of the power law exponent

Regression fits on a log-log scale may produce inaccurate estimates of power law exponents. For this reason, Clauset *et al.* [35] proposed the following maximum likelihood estimator to determine both the exponent γ and minimum diameter D_{min} of powerlaws more accurately:

$$\gamma = 1 + n \left[\sum_{i=1}^{n} \ln \left(\frac{D_i}{D_{min}} \right) \right]^{-1} \tag{31}$$

where D_i and n represent the diameter of the i-th fragment and the total number of fragments, respectively. The value of D_{min} is chosen so as to minimize the Kolmogorov Smirnov statistic with respect to the input dataset [35]. In the current work, the dedicated python package [36] *power law* is used to evaluate eq. 31.

Unfortunately, the number of fragment size samples provided by Reitter *et al.* [27] for each of their impact experiments (about 200) appears insufficient to apply the methodology described above. On the contrary, consistent results could be obtained for the experiments of Vargas *et al.* [9] as their data comprises about 2000 samples per impact. Finally, the use of the statistical tools of Clauset *et al.* [35] requires access to the raw fragment size data, which is not available for the experiments of Guégan *et al.* [12]. Therefore,

this method may only be applied for the experiments of Vargas *et al.* [9], while a less precise regression approach must be employed for the datasets of Reitter *et al.* [27] and Guégan *et al.* [12].

The uncertainty on power law exponent estimates obtained from regressions on a log-log scale may be reduced by fitting cumulated volume distributions as they generally display lower statistical fluctations [35, 36]. In addition, a regression method adapted to the presence of outliers and implemented in python's scikit-learn library and known as 'RANdom SAmple Consensus' (RANSAC) is used [37]. The use of such method appears necessary as the fragment volume data does not follow a power law for the smallest fragment sizes, possibly due to resolution limitations inherent to such experiments.

The exponent of the cumulated volume distribution function $\delta = \gamma + 1$ deduced for the different experiments is shown in fig 6. Considering the data of Vargas *et al.* [9], it appears that either estimates of the exponent, namely the RANSAC regressor [37] or the maximum likelihood estimator of Clauset *et al.* [35], yield very similar results. Since each impact experiment was repeated about 10 times in the experiments of Vargas *et al.* [9], an average over the repetitions could be performed to evaluate the exponent γ. This probably explains the low dispersion for the data of Vargas *et al.* [9] as the exponents cluster within the range $[1.1 - 1.4]$. More generally, no clear trend regarding the evolution of the exponent with normal impact velocity seems visible for any of the data sets and the same remark holds for the impact diameter (not shown). Therefore, an average value is used for the power law exponent, yielding $\delta \approx 1.27$, close to the value reported for glass

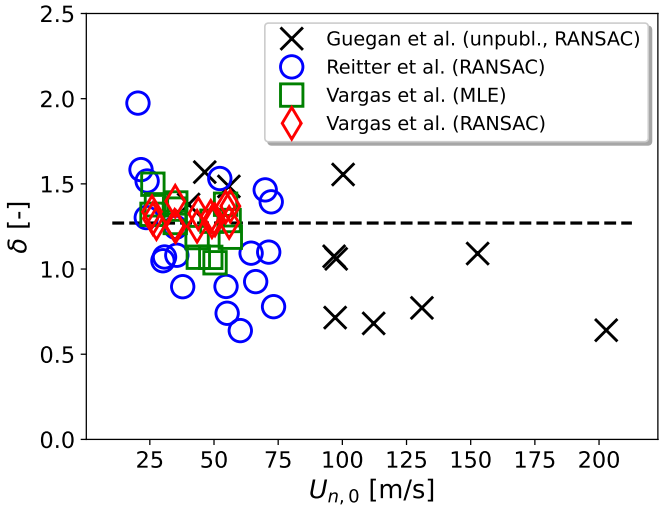

Figure 6: Exponent of the cumulated volume size distribution as a function of the normal impact velocity for the different experimental datasets. For the experimental data of Vargas *et al.* [9], results are computed with both the maximum likelihood estimator of Clauset *et al.* [35] and the RANSAC regressor [37].

fragmentation in Kolsky torsion bar experiments [38]. Similarly, the ratio between the minimum diameter and the initial diameter is approximately constant on average, $D_{min}/D_0 \approx 0.052$.

3.5. Fit evaluation

The quality of the proposed fits is illustrated by comparison to experimental cumulated volume distributions for moderate, intermediate and large impact velocities in figs. 7, 8 and 9. The data respectively correspond to distributions obtained from the experiments of Reitter *et al.* [27] (moderate impact velocity), Vargas *et al.* [9] (intermediate) and Guégan *et al.* [12] (large). In each case, distributions obtained for two almost identical impact

conditions are shown to illustrate their variability. Finally, the cumulated volume distributions predicted by the model of Pan and Render [10] are shown for comparison. Pan and Render [10] assume the fragment volume distribution to follow a Weibull distribution, see eq. 24. They express the parameters of their Weibull distribution as:

$$\frac{\lambda^{pr}}{D_0} = 0.3 - \left(\frac{U_{n,0}}{a_L}\right)^2 \tag{32}$$

$$\beta^{pr} = 3.512 - 4\left(\frac{U_{n,0}}{a_L}\right) \tag{33}$$

with $a_L = 340\,\mathrm{m\,s^{-1}}$ a reference value for the speed of sound. The strict positivity constraint on these parameters limits the validity of relations 32-33 to $U_{n,0} < 186\,\mathrm{m\,s^{-1}}$ approximately.

The cumulated volume distributions are either found to be "s-shaped", see fig. 7a, or "upward concave", see fig. 7b. The "s-shaped" may best be reproduced with the lognormal law for the present fits. On the contrary, they are not well reproduced by the current Weibull fit because of the truncation performed at the predicted maximum fragment diameter. The fit proposed by Pan and Render [10] predicts comparatively larger shape parameters and results in cumulated volume distributions that are not truncated, hence "s-shaped". Finally, the current power law fit may only reproduce "upward concave" cumulated volume distributions. It appears from all figures that there is significant variability in the distributions, apparently resulting in different best fit candidates, even for almost identical conditions, see for instance figs. 7a and 7b. Since the current fits are all normalized by the current maximum fragment diameter estimate, they are inherently sensitive to errors of the latter, as may be seen from fig. 9a.

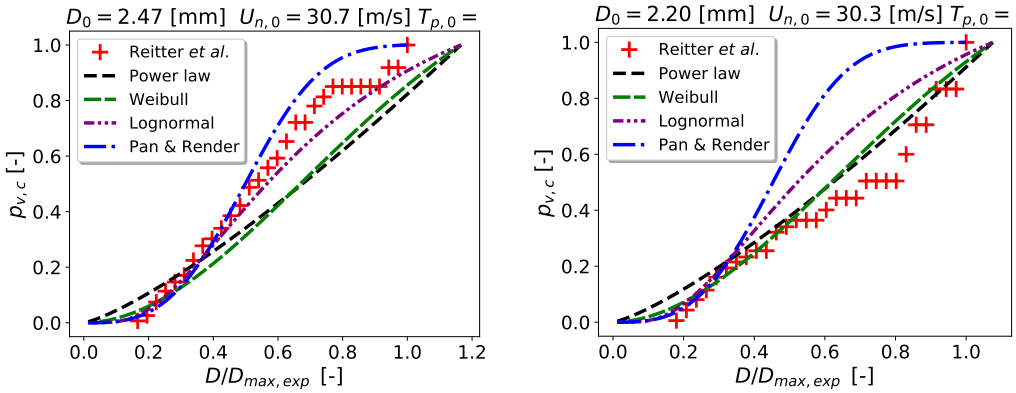

(a) (b)

Figure 7: Experimental and model cumulated volume distributions from the experiments of Reitter *et al.* [27], comprising the power law, Weibull and lognormal fits of the present work as well as the Weibull law proposed by Pan and Render [10]. The impact parameters are provided above each plot.

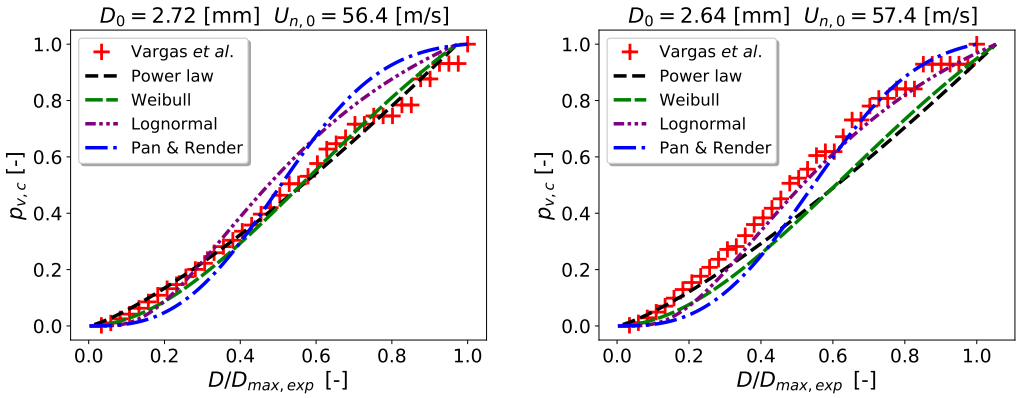

(a) (b)

Figure 8: Experimental and model cumulated volume distributions from the experiments of Vargas *et al.* [9], comprising the power law, Weibull and lognormal fits of the present work as well as the Weibull law proposed by Pan and Render [10]. The impact parameters are provided above each plot.

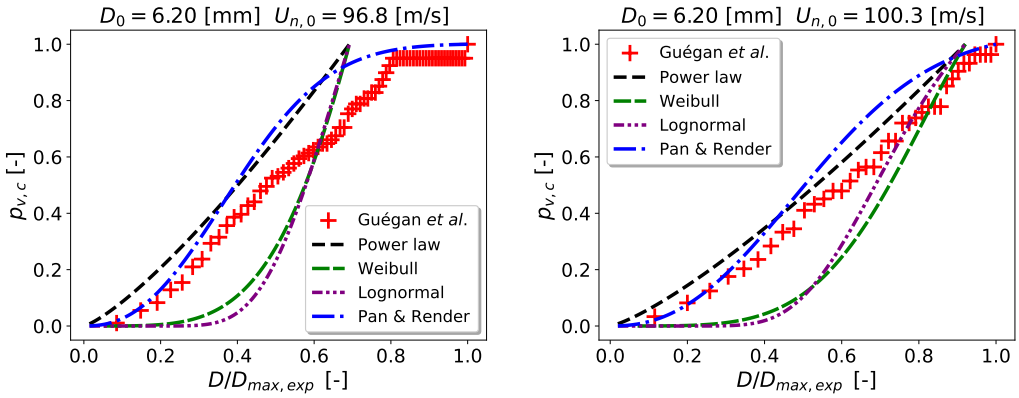

(a) (b)

Figure 9: Experimental and model cumulated volume distributions from the experiments of Guégan *et al.* [12] (previously unpublished data), comprising the power law, Weibull and lognormal fits of the present work as well as the Weibull law proposed by Pan and Render [10]. The impact parameters are provided above each plot.

In order to provide a more quantitative analysis, the average errors for the Sauter mean diameter D^n_{32}, volume mean diameter D^n_{43} as well as the D^v_{10}, D^v_{50} and D^v_{90} diameters are given in tables 4, 5 and 6, respectively for the data of Reitter *et al.* [27], Vargas *et al.* [9] and Guégan *et al.* [12]. The trends are somewhat similar for the data of Reitter *et al.* [27], Vargas *et al.* [9], both in terms of error levels and candidate fits. For these experiments, the current Weibull fit seems the best approximation to the fragment volume data. While this behavior is expected for the D^n_{32} and D^n_{43} diameters given the fitting strategy exposed in section 3.2, the low error levels observed on the D^v_{10}, D^v_{50} and D^v_{90} diameters confirm its ability to reproduce the experimental distributions with good accuracy. These conclusions do not apply for the data of Guégan *et al.* [12]. First, the fitting strategy proposed for the lognormal and Weibull laws suffers from the inability to accurately predict

the experimental D_{32}^n and D_{43}^n diameters for the data of Guégan *et al.* [12] using relations 29 and 30. The associated error levels may then be either mitigated or further enhanced given the maximum diameter estimate used for normalization. The lognormal and Weibull laws predict excessively "upward concave" shapes for the data of Guégan *et al.* [12], resulting in huge errors on the D_{10}^v, while recovering satisfactory error levels for the remaining quantities. More generally, no clear trend in favor of any distribution seems visible for the data of Guégan *et al.* [12]. Because of a much more simple design, namely a maximum diameter estimate that seems accurate on average and a constant exponent obtained via averaging the entire size distribution data, the power law appears as the most robust distribution over the three experimental datasets, at the cost of larger error levels, in particular on the D_{32}^n diameter. While the Weibull fit of Pan and Render [10] also shows remarkable accuracy for the data of Reitter *et al.* [27] and Vargas *et al.* [9], it may not be extrapolated towards the largest normal impact velocities representative of engine ice crystal icing.

Experiments of Reitter *et al.* [27]	Average errors [%]				
	D_{32}^n	D_{43}^n	D_{10}^v	D_{50}^v	D_{90}^v
Pan and Render [10], Weibull law	16.07	19.71	22.52	18.61	20.95
Current, power law	30.78	24.95	26.49	17.45	17.03
Current, Weibull law	**12.62**	**12.14**	19.84	17.08	16.31
Current, lognormal law	14.05	13.39	**19.22**	**13.27**	**14.38**

Table 4: Average errors on the Sauter mean diameter D_{32}^n, volume weighted mean diameter D_{43}^n, the D_{10}^v, D_{50}^v and D_{90}^v diameters for the model of Pan and Render [10] as well as the present power, Weibull and lognormal laws for the experimental data of Reitter *et al.* [27]. The minimum average error in each column is displayed in bold.

Experiments of Vargas *et al.* [9]	Average errors [%]				
	D_{32}^n	D_{43}^n	D_{10}^v	D_{50}^v	D_{90}^v
Pan and Render [10], Weibull law	15.68	28.45	37.02	24.37	28.48
Current, power law	32.06	**15.03**	**16.89**	13.93	**15.07**
Current, Weibull law	**12.22**	17.02	22.46	**13.91**	15.59
Current, lognormal law	13.16	23.67	20.01	22.53	17.66

Table 5: Average errors on the Sauter mean diameter D_{32}^n, volume weighted mean diameter D_{43}^n, the D_{10}^v, D_{50}^v and D_{90}^v diameters for the model of Pan and Render [10] as well as the present power, Weibull and lognormal laws for the experimental data of Vargas *et al.* [9]. The minimum average error in each column is displayed in bold.

Experiments of Guégan *et al.* [12]	Average errors [%]				
	D_{32}^n	D_{43}^n	D_{10}^v	D_{50}^v	D_{90}^v
Pan and Render [10], Weibull law	56.82	46.85	**34.05**	26.92	21.52
Current, power law	37.87	29.33	42.55	**18.21**	17.59
Current, Weibull law	20.07	**21.64**	91.16	21.85	14.96
Current, lognormal law	**17.87**	23.30	105.89	18.52	**14.80**

Table 6: Average errors on the Sauter mean diameter D_{32}^n, volume weighted mean diameter D_{43}^n, the D_{10}^v, D_{50}^v and D_{90}^v diameters for the present fits as well as the model of Pan and Render [10] for the experimental data of Guégan *et al.* [12]. The minimum average error in each column is displayed in bold.

4. Conclusion

The fragmentation of ice particles resulting from their impact on solid walls was examined in an attempt to model size characteristics of the reemited fragments. First, a new semi-empirical model predicting the diameter of the largest reemited fragment was proposed. The strong compression resulting from impact is assumed to remain limited to the vicinity of the contact area, while inducing increasing tensile strain elsewhere, resulting in crack formation and eventually fragmentation. Accordingly, an energy formalism considering fragmentation to be driven by the conversion of tensile and kinetic energies into fracture surface energy was applied. The tensile strain causing fragmentation was related to the indentation radius in the contact area assuming plastic deformation. The resulting model may incorporate strain rate and temperature dependent compressive yield strength as well as a temperature dependent surface fracture energy. Model predictions appear in good agreement with all considered experimental data, thus covering broad normal impact velocity ([20-200 $\mathrm{m\,s^{-1}}$]) and initial particle diameter ([30 µm-20 mm]) ranges.

Modeling of the fragment volume distribution was then considered. In particular, the respective accuracy of power, lognormal and Weibull laws was evaluated to determine the best fitting candidate to the present fragment volume data. For the lognormal and Weibull laws, the fitting strategy is based on an estimate of the Sauter mean diameter and the mean volume diameters using the previously derived strain rate estimate. For the power law, a maximum likelihood estimator was used to determine its exponent when possible. Alternatively, a regression method adapted to the presence

of outliers on a log-log scale was applied. The current Weibull fit seems best suited to approximate the impact data up to moderate impact velocities, i.e. up to $80\,\mathrm{m\,s^{-1}}$. However, this fit yields huge errors in the low diameter range of the fragment volume distributions at higher normal impact velocities. In particular, average errors on the D_{10}^{v} diameter are unacceptably large for the current Weibull and lognormal fits. This is mainly due to the fact that the current Sauter mean and mean volume diameter estimates, which the current Weibull and lognormal fits are based on, exhibit large errors when extrapolated to higher impact velocities. Due to these uncertainties, a simple power law fit based on a constant exponent seems to yield higher yet more stable average error levels over the entire available fragment volume data. The fragment volume distribution fit proposed by Pan and Render [10] performs almost as well as the current Weibull fit for the moderate impact velocity fragment data. As for the current fits, the accuracy of Pan and Render's fit deteriorates when considering fragment distribution data at higher impact velocities, in particular for the Sauter mean and volume mean diameters. Moreover, the fragment volume distribution model of Pan and Render may not cover the entire normal impact velocity range representative of ice crystal icing (50-250 $\mathrm{m\,s^{-1}}$ approximately) as it loses validity for normal impact velocities exceeding $186\,\mathrm{m\,s^{-1}}$.

Considering the outlooks, it seems worthwhile to further confirm the main underlying assumption of a link between the indentation radius and the tensile strain magnitude causing fragmentation. Detailed numerical simulations of ice particle impact seem best suited for such purpose. Regarding the fragment volume distributions, it seems important to gather additional fragment

data for high velocity impacts to assess whether the resulting volume distributions follow significantly different trends. More generally, a better characterization and understanding of the statistical variability of experimental impact data with respect to impact parameters seems crucial to improve modeling accuracy.

Acknowledgement

The funding received within the European Union's Horizon 2020 research and innovation programm under grant agreement No 767560 is gratefully acknowledged. The authors also thank Dr. Paul Tsao for his valuable comments on the manuscript.

Appendix A. Accounting for varying material properties

The energy per unit area required to create new fracture surface G_c is assumed to depend on the material temperature [15]:

$$G_c = G_{c,0} \exp\left(\frac{Q_s}{\mathcal{R}T} - \frac{Q_s}{\mathcal{R}T_0}\right) \tag{A.1}$$

with $G_{c,0} = 0.12\,\mathrm{J\,m^{-2}}$ representing the reference surface energy per unit area [22], $T_0 = 253\,\mathrm{K}$ the reference temperature, $Q_s = 4.82 \times 10^4\,\mathrm{J\,mol^{-1}}$ the reference activation energy [39] and $\mathcal{R} = 8.314\,\mathrm{J\,mol^{-1}\,K^{-1}}$ the universal molar gas constant.

Regarding the compressive yield strength, experimental evidence suggests that it depends on both strain rate and temperature [13, 21]. Regarding strain rate dependency, a polynomial fit to the average curve given by Tippmann [13] and gathering experimental measurements from several sources

is used. The temperature dependency of the quasi-static compressive yield strength of ice is described with the experimental data compiled by Petrovic [21]. It appears that a simple linear fit yields a satisfactory accuracy for the latter quantity. The resulting expression reads:

$$Y_c(T, \dot{\varepsilon}) = Y_{c,0} f_{y_c}(\dot{\varepsilon}) g_{y_c}(T) \tag{A.2}$$

with:

$$\begin{aligned} f_{y_c}(\dot{\varepsilon}) &= \exp\Big(3.595 \times 10^{-4} \ln^3(\dot{\varepsilon}/\dot{\varepsilon}_0) - 7.470 \times 10^{-3} \ln^2(\dot{\varepsilon}/\dot{\varepsilon}_0) \\ &+ 1.118 \times 10^{-1} \ln(\dot{\varepsilon}/\dot{\varepsilon}_0) + 1.062\Big) \qquad \text{(A.3)} \\ g_{y_c}(T) &= -28.70\,(T/T_{c,0}) + 30.21 \qquad \text{(A.4)} \end{aligned}$$

with $Y_{c,0} = 5.2 \times 10^6\,\mathrm{Pa}$ representing a reference value for the quasi-static compressive yield strength at $T_{c,0} = 273\,\mathrm{K}$ [13, 21]. The maximum error remains below 2% for the strain rate dependency with respect to the numerized data of Tippmann [13] and below 0.5% for the temperature dependency with respect to the numerized data of Petrovic [21]. Note that the use of eq. A.2 requires an iterative procedure to determine the characteristic strain rate in eq. 12.

References

[1] J. W. Strapp, M. Bravin, J. Mason, An investigation into location and convective lifecycle trends in an ice crystal icing engine event database, in: SAE 2015 International Conference on Icing of Aircraft, Engines, and Structures, SAE International, 2015.

[2] T. C. Currie, D. Fuleki, Experimental results for ice crystal icing on hemispherical and double wedge geometries at varying mach numbers and wet bulb temperatures, in: 8th AIAA Atmospheric and Space Environments Conference, 2016, p. 3740.

[3] F. Dezitter, A. Grandin, J. L. Brenguier, F. Hervy, H. Schlager, P. Villedieu, G. Zalamansky, HAIC-High Altitude Ice Crystals, in: 5th AIAA Atmospheric and Space Environments Conference, 2013, p. 2674.

[4] P. Trontin, P. Villedieu, A comprehensive accretion model for glaciated icing conditions, International Journal of Multiphase Flow 108 (2018) 105–123.

[5] EU-Comission, MUSICHAIC: 3D MUltidisciplinary tools for the Simulation of In-flight iCing due to High Altitude Ice Crystals, `https://www.music-haic.eu/`, accessed: 2021-08-06 (2020).

[6] W. B. Wright, P. Struk, T. Bartkus, G. Addy, Recent advances in the Lewice icing model (2015).

[7] P. Trontin, G. Blanchard, A. Kontogiannis, P. Villedieu, Description and assessment of the new onera 2d icing suite igloo2d, in: 9th AIAA Atmospheric and Space Environments Conference, 2017, p. 3417.

[8] T. Hauk, E. Bonaccurso, I. Roisman, C. Tropea, Ice crystal impact onto a dry solid wall. particle fragmentation, Proceedings of the Royal Society A: Mathematical, Physical and Engineering Sciences 471 (2181) (2015) 20150399.

[9] M. M. Vargas, C. R. Ruggeri, M. Pereira, D. Revilock, Fragment size distribution for ice particle impacts on a glass plate, in: 2018 Atmospheric and Space Environments Conference, 2018, p. 4225.

[10] H. Pan, P. Render, Impact characteristics of hailstones simulating ingestion by turbofan aeroengines, Journal of Propulsion and Power 12 (3) (1996) 457–462.

[11] P. Guegan, R. Othman, D. Lebreton, F. Pasco, P. Villedieu, J. Meyssonnier, S. Wintenberger, Experimental investigation of the kinematics of post-impact ice fragments, International Journal of Impact Engineering 38 (10) (2011) 786–795.

[12] P. Guegan, R. Othman, D. Lebreton, F. Pasco, P. Villedieu, J. Meyssonnier, S. Wintenberger, Size distribution data of post-impact ice fragments, unpublished data (2011).

[13] J. D. Tippmann, H. Kim, J. D. Rhymer, Experimentally validated strain rate dependent material model for spherical ice impact simulation, International Journal of Impact Engineering 57 (2013) 43–54.

[14] H. Carmona, F. Wittel, F. Kun, H. J. Herrmann, Fragmentation processes in impact of spheres, Physical Review E 77 (5) (2008) 051302.

[15] P. Villedieu, P. Trontin, R. Chauvin, Glaciated and mixed phase ice accretion modeling using onera 2d icing suite, in: 6th AIAA atmospheric and space environments conference, 2014, p. 2199.

[16] J. Weiss, Fracture and fragmentation of ice: a fractal analysis of scale invariance, Engineering Fracture Mechanics 68 (17-18) (2001) 1975–2012.

[17] D. Grady, The spall strength of condensed matter, Journal of the Mechanics and Physics of Solids 36 (3) (1988) 353–384.

[18] D. Grady, Physics of Shock and Impact, Vol. 1, Chapter 2, pp. 71–74, IOP Publishing, London, 2017.

[19] I. Hutchings, Strain rate effects in microparticle impact, Journal of Physics D: Applied Physics 10 (14) (1977) L179.

[20] I. Roisman, C. Tropea, Impact of a crushing ice particle onto a dry solid wall, Proceedings of the Royal Society A: Mathematical, Physical and Engineering Sciences 471 (2183) (2015) 20150525.

[21] J. Petrovic, Review mechanical properties of ice and snow, Journal of materials science 38 (1) (2003) 1–6.

[22] G. Vidaurre, J. Hallett, Particle impact and breakup in aircraft measurement, Journal of Atmospheric and Oceanic Technology 26 (5) (2009) 972–983.

[23] L. Glenn, A. Chudnovsky, Strain-energy effects on dynamic fragmentation, Journal of Applied Physics 59 (4) (1986) 1379–1380.

[24] J. Pernas-Sánchez, D. Pedroche, D. Varas, J. López-Puente, R. Zaera, Numerical modeling of ice behavior under high velocity impacts, International Journal of Solids and Structures 49 (14) (2012) 1919–1927.

[25] H. Park, H. Kim, Damage resistance of single lap adhesive composite joints by transverse ice impact, International Journal of Impact Engineering 37 (2) (2010) 177–184.

[26] N. Karpen, A. Cuco, D. Kuenstler, E. Bonaccurso, MUSIC-haic_WP1_T11_ACRT_01_ParticleImpactOnRigidSurface (Oct. 2021). doi:10.5281/zenodo.5576280.

[27] L. M. Reitter, M. Schremb, H. Lohmann, I. Roisman, J. Hussong, C. Tropea, MUSIC-haic_WP1_T11_TUDA_01_ParticleImpactOnRigidColdSurface (1.0.0) [data set]. Zenodo. (2021). doi:10.5281/zenodo.5575128.

[28] N. Karpen, A. Cuco, D. Kuenstler, E. Bonaccurso, L. M. Reitter, I. V. Roisman, C. Tropea, Characterizing microscopic ice particle impacts onto a rigid surface: Wind tunnel setup and analysis, in: AIAA AVIATION 2021 FORUM, August 2021. doi:10.2514/6.2021-2671.

[29] E. Sharon, S. P. Gross, J. Fineberg, Energy dissipation in dynamic fracture, Physical review letters 76 (12) (1996) 2117.

[30] D. Turcotte, Fractals and fragmentation, Journal of Geophysical Research: Solid Earth 91 (B2) (1986) 1921–1926.

[31] J. E. Funk, D. R. Dinger, Predictive process control of crowded particulate suspensions: applied to ceramic manufacturing, Springer Science & Business Media, 2013.

[32] D. Grady, Fragment size distributions from the dynamic fragmentation of brittle solids, International Journal of Impact Engineering 35 (12) (2008) 1557–1562.

[33] A. Fowler, B. Scheu, A theoretical explanation of grain size distributions in explosive rock fragmentation, Proceedings of the Royal Society

A: Mathematical, Physical and Engineering Sciences 472 (2190) (2016) 20150843.

[34] L. M. Reitter, M. Schremb, H. Lohmann, C. Tropea, Experimental investigation of ice particle impacts onto a rigid substrate, in: AIAA 2021-2670, AIAA AVIATION 2021 FORUM, August 2021. doi:10.2514/6.2021-2670.

[35] A. Clauset, C. R. Shalizi, M. E. Newman, Power-law distributions in empirical data, SIAM review 51 (4) (2009) 661–703.

[36] J. Alstott, E. Bullmore, D. Plenz, powerlaw: a python package for analysis of heavy-tailed distributions, PloS one 9 (1) (2014) e85777.

[37] M. A. Fischler, R. C. Bolles, Random sample consensus: a paradigm for model fitting with applications to image analysis and automated cartography, Communications of the ACM 24 (6) (1981) 381–395.

[38] L. Costin, D. Grady, Dynamic fragmentation of brittle materials using the torsional kolsky bar, Tech. rep., Sandia National Labs., Albuquerque, NM (USA) (1984).

[39] M. Higa, M. Arakawa, N. Maeno, Size dependence of restitution coefficients of ice in relation to collision strength, Icarus 133 (2) (1998) 310–320.